![USGS logo - science for a changing world]

An interpretation of the 1996 aeromagnetic data for the Santa Cruz basin, Tumacacori Mountains, Santa Rita Mountains, and Patagonia Mountains, south-central Arizona

By Mark E. Gettings[1]

U. S. DEPARTMENT OF THE INTERIOR
U.S. GEOLOGICAL SURVEY

[1]U.S. Geological Survey, Tucson, Arizona

Table of Contents

Figures

2c. Plot of trend segment lengths versus trend segment azimuth.

3. Three functions with identical mean and standard deviation. Functions are a straight line, a sine curve, and fractional Brownian motion of dimension $D = 1.70$.

4. Example of the calculation of the textural measures number of peaks and troughs per km and Euclidean length per km for two successive windows five points wide moving two data points at a time.

5. Aeromagnetic anomaly data from one line of a high resolution aeromagnetic survey.

6. Number of peaks and troughs per km for the data of figure 4 for four different window widths.

7. Euclidean length per km in units of the square root of km squared plus nanoTeslas squared for the data of figure 4 for four different window widths.

8. Matrix diagram showing the ranking scheme used to categorize the number of peaks and troughs grid and the Euclidean length grid into a single grid.

Plates

1. Santa Cruz Valley geologic map, including the Santa Cruz Valley and the surrounding Tumacacori, Santa Rita, and Patagonia Mountains.

2. Shaded relief aeromagnetic data with linework from the geologic map.

3. Shaded relief aeromagnetic data with geologic linework and faults, trends and boundaries inferred from the aeromagnetic data.

4. Randomly colored gridded aeromagnetic data with some inferred boundaries.

5. Number of peaks and troughs per kilometer of the magnetic anomaly field.

6. Euclidean length per kilometer of the magnetic anomaly field.

7. Ranked Euclidean length and number of peaks and troughs of the magnetic anomaly field.

Appendices

1. Postscript files of: 1) contour maps of parts of the aeromagnetic survey to overlay the 1:48,000 scale geologic maps of Drewes (1971) and Simons (1974); and 2) 1:175,000 scale versions of the color plates 1-7.
2. FORTRAN source code of program used to calculate the textural measures.

Abstract

High resolution aeromagnetic survey data flown at 250 m above the terrain and 250 m line spacing over the Santa Cruz Valley and the surrounding Tumacacori, Patagonia, and Santa Rita Mountains has been interpreted by correlation of the magnetic anomaly field and various derivative maps with geologic maps. Measurements of in-situ magnetic properties of several of the map units determined whether or not mapped lithologies were responsible for observed anomalies. Correlation of the magnetic anomaly field with mapped geology shows that numerous map units of volcanic and intrusive rocks from Jurassic Middle Tertiary in age are reversely polarized, some of which have not been previously reported. Trends derived from the magnetic anomaly data correlate closely with structures from major tectonic events in the geologic history of the area including Triassic-Jurassic crustal accretion and magmatism, Laramide magmatism and tectonism, northeast-southwest Mid-Tertiary extension, and east-west Basin and Range extension. Application of two textural measures to the magnetic anomaly data, number of peaks and troughs per km (a measure of roughness) and Euclidean length per km (a measure of amplitude), delineated areas of consistent magnetic anomaly texture. These measures were successful at the delineation of areas of consistent magnetic lithology both on the surface and in the subsurface beneath basin fill. Several areas of basement prospective for mineral resources beneath basin fill were identified.

Introduction

A high resolution aeromagnetic survey was flown over the Patagonia Mountains, Santa Rita Mountains, upper Santa Cruz Valley, and Tumacacori Mountains (figure 1) in late 1996 and early 1997 under contract for the U.S. Geological Survey. The data are available to the public via the Worldwide Web (Sweeney, 2000). Phillips (2001) describes the processing of this data into a final corrected flight line dataset used for the work described here. This dataset was used to prepare maps of the aeromagnetic anomaly field and derivative maps of textural measures that were correlated with published geological maps to yield the interpretation described in this report. Measurements of in-situ magnetic properties at a number of sites in the survey area were completed to help constrain interpretations and provide model susceptibility values.

Previous studies of the aeromagnetic field in the area include the aeromagnetic map for the state of Arizona (Sauck and Sumner, 1970), Ponce (1990), and Gettings (1996). Proprietary aeromagnetic data flown by a consortium of mineral exploration companies includes the eastern 20% of the survey area. Primary sources of geologic data for this study include Drewes (1971, 1980, 1996), Simons (1974), and Gettings and Houser (1997).

This report introduces several new techniques for characterizing the texture of magnetic field data in ways that can be used for correlation with lithology and geologic structure. In order to focus on the techniques, the author has chosen to organize the report by subject rather than by geographic area or geologic features. Thus, some areas will be discussed several times at different places in the report as the results of the application of the various techniques are discussed. For each technique, a catalog style keyed to the map plates was used and in general, the order of discussion is the order of the numbered areas or anomalies on the map plates. This organization allows the reader to ascertain from which technique a particular interpretive feature was derived and to judge the relative effectiveness of techniques. Not all anomalies or magnetic field features have been interpreted or discussed; the dataset contains a great richness of detail that is beyond the scope of this study to interpret in its entirety. It is the author s hope that the most important features have been discussed.

After the presentation of the field measurements of magnetic property data, a comparison of the aeromagnetic anomaly data with the geologic map data is given. This is followed by a trend or lineament analysis of the aeromagnetic anomaly data. Next comes a discussion of the techniques of quantifying two textural measures of the aeromagnetic data and an analysis of the textural measures applied to the aeromagnetic dataset of this study. The report concludes with some generalizations and suggestions for further work.

Figure 1
Location of the study area.

Contour interval is 100 meters
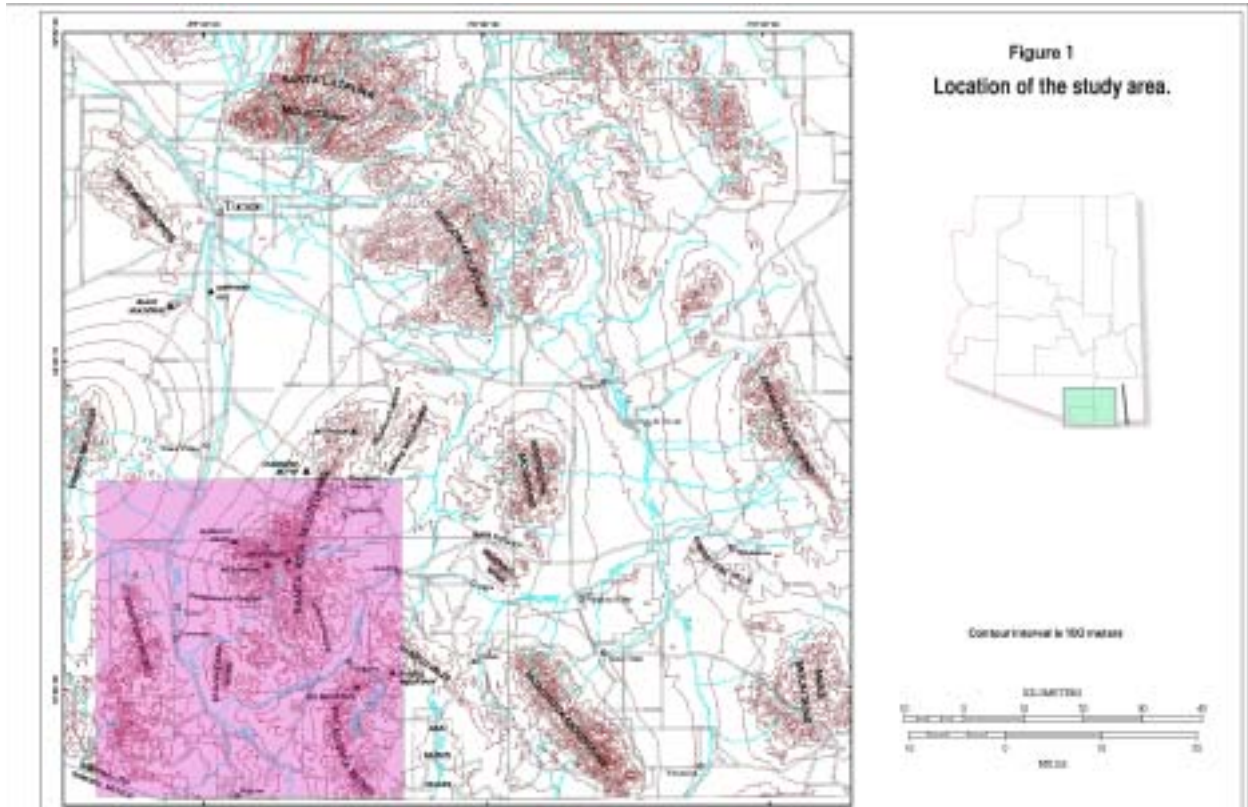
Magnetic property data

Measurements of rock magnetic susceptibility, remanent polarity, or both, were completed at 35 sites within the study area, of which 20 are susceptibility only. The results of these measurements are presented in tabular form in Table 1 and the distribution of sites is shown on the Plate 1. Magnetic susceptibility was measured using a Sapphire Instruments model SI-1 equipped with a 20x20 cm flat field coil designed for measurements on outcrops. Remanent magnetic polarities were measured using several fluxgate magnetometers made by California Instruments (model 70 magnetometer). The use of brand names in this document is for descriptive purposes only and does not constitute endorsement. For the polarity measurements, oriented hand samples of 0.5 to 5 kg mass were used. Care was taken in collection of oriented samples to sample from areas which appeared to be protected from lightning strikes. Most specimens were measured for polarity at least twice to minimize errors in direction of polarization. Directions of magnetization determined for hand samples are probably accurate to

about ±10° in any plane, but demagnetization effects for any given specimen due to sample shape and heterogeneous distribution of magnetic minerals may increase the uncertainty. In general, the susceptibility measurements are probably accurate to about $\pm1.0\times10^{-6}$ cgs/cc (cubic centimeter) or better, with a standard deviation of repeated measurements of about 0.4% of the mean susceptibility (Gettings and others, 1994). The field coil for the SI-1 measures the average susceptibility for a 20 by 20 cm area to a depth of about 15 cm, thus the measurements sample about a 6000 cc volume. Most outcrops measured were about 2 by 3 m in size with the five sample spots essentially randomly distributed over the outcrop. Site latitude, longitude, and altitude were obtained from Global Positioning System (GPS) measurements or from 1:24,000 scale topographic maps. The GPS horizontal locations are accurate to about ±10m, and the GPS altitudes are probably accurate to ±20m. For locations from maps, the horizontal uncertainty is about ±20m, and vertical uncertainty is about ±7m.

In this report, the terminology reversely polarized or similar terms will be used to describe magnetization directions which are other than in the direction of the present day magnetic (induction) field. This includes directions which are other than anti-parallel to the present day field, such as in a magnetic east or west direction. Rock magnetization directions that are along or nearly along the present day field direction will be termed normally polarized or with a similar term. The measurements show that rocks of several ages are reversely polarized, and this is borne out by examination of the aeromagnetic map (pl. 2). The Squaw Gulch granite batholith (Drewes, 1971; unit Jg at sites 4 and 5 on pl. 1; area around no. 7 on pl. 2) of Jurassic age is reversely polarized and forms the basement for much of the central part of the map area. Upper Cretaceous dacite flows and tuffs of the lower member of the Salero Formation (Drewes, 1971; unit Krt on pl. 1 at site 3; area around no. 8 on pl. 2) are reversed while the upper welded tuff member is normally polarized (pl. 1 at site no. 2). The upper Cretaceous Josephine Canyon diorite (Drewes, 1971; Kj on pl. 1 at site 6; no. 2 on pl. 2) is younger (about 65 Ma) and is normally polarized. This rock has a strong remanent magnetization as well as a large susceptibility and is responsible for many of the strong positive magnetic anomalies in the study area. The Gringo Gulch pluton (Drewes, 1971; unit TKg on pl. 1 at sites 8-10; no. 11 on pl. 2) is slightly younger (Lower Paleocene, Vugteveen and others, 1981) and is normally polarized, but contains a reversely polarized late phase microgranodiorite (also reported in Hagstrum, 1994).

Both the Josephine Canyon diorite and the Gringo Gulch pluton are part of the Laramide magmatic episode that resulted in many diorite and granodiorite intrusions in southeast Arizona (Dickinson, 1989). Many of these intrusions are associated with the porphyry copper deposits of southeast Arizona

Table 1. Measured magnetic susceptibility and remanent magnetic polarity at selected sites.

[Map unit symbols and formation names refer to units on geologic maps by Drewes (1971, 1980) and Simons (1974). UTM northing and easting are Universal Transverse Mercator coordinates for zone 12N for the sample site. N is the number of susceptibility measurements on different areas of the outcrop at each site. Abbreviations in Remanent Polarity describe directions very different from normal or reversed, for example, `flat90dEoMN` means flat (horizontal) 90 degrees east of magnetic north ; na, not available. Sample ID refers to the sample location plotted on Plate 1. The last 20 sites in the table were measured only for susceptibility and the maximum and minimum values are given in addition to mean and standard deviation. The instrument used for these sites was a KT-6 Kappa meter, with similar accuracy and precision to the SI-1 described in the text but measuring a smaller volume of rock, about 500 cc.]

Map unit	Lithology	UTM Easting (m)	UTM Northing (m)	Altitude (ft)	Mean magnetic Susceptibility K, cgs/cc	Standard deviation	N	Remanent Polarity **N**ormal/ **R**eversed	Remanent Intensity weak moderate strong	Sample ID
Tgd_a	agglomerate	501154e	3505133n	3665f	2.99e-4	1.88e-4	15	N	weak	1
Ksw	Salero welded tuff	505871e	3501793n	4265f	7.80e-4	1.16e-4	5	N(flat90 dEoMN)	moderate	2
Kse	Salero megabreccia	506995e	3501570n	4386f	1.39e-5	1.74e-6	5	R(flat90 dWoMN)	very weak	3
Js	Squaw Gulch granite	516383e	3493614n	4775f	9.23e-4	1.02e-4	5	R(steepW oMN)	moderate	4
Js	Squaw Gulch granite	515315e	3493422n	4805f	5.74e-4	4.30e-5	5	R(steepW oMN)	moderate	5
Kj	Josephine Canyon diorite	515652e	3492991n	4791f	2.404e-3	2.26e-4	5	N(60dEoM N)	strong	6
Tgut	Gringo Volcanics rhyolite tuff	521882e	3493885n	4433f	7.14e-6	2.52e-5	5	na	na	7
Tgm	micrograndiorite	520994e	3494288n	4627f	2.75e-3	1.13e-4	5	R	weak/ moderate	8
Tgm	micrograndiorite	520991e	3494066n	4453f	3.63e-3	1.60e-4	5	R	strong	9
Tgdp	diorite porphyry	521085e	3493771n	4539f	2.13e-3	3.24e-4	5	N(flat)	strong	10
Kbm_w	Bathtub rhyolite welded tuff	521393e	3493766n	4684f	9.72e-6	2.21e-6	5	R(upEoMS)	moderate	11
Kbm	Bathtub hornblende dacite	521425e	3494728n	4785f	1.13e-3	9.18e-5	5	?	?	12
Kbm	Bathtub gray tuff breccia	521899e	3494595n	4439f	5.47e-4	7.80e-5	5	?	?	13
Trp	Piper Gulch monzonite	516910e	3498422n	5435f	2.09e-3	3.53e-4	5	?	?	14
Klp	Quartz latite porphyry	518580e	3497900n	4721f	1.26e-5	3.02e-6	5	?	?	15

Map unit	Lithology	UTM Easting (m)	UTM Northing (m)	Altitude (ft)	Mean magnetic Susceptibility K, cgs/cc	Standard deviation	N	Minimum K	Maximum K	Sample ID
Tuc	Nogales conglomerate	479901e	3513797n	3595f	1.05e-04	2.40e-05	6	6.21e-05	1.33e-04	16
Kr	Rhyodacite welded tuff	478388e	3519766n	3990f	8.22e-06	3.25e-06	6	3.18e-06	1.19e-05	17
Kr	Rhyodacite welded tuff	478288e	3519813n	4020f	5.41e-06	3.79e-06	5	7.96e-07	1.11e-05	18
Kr	Andesite tuff breccia	478600e	3521805n	4115f	1.58e-05	1.84e-06	6	1.35e-05	1.83e-05	19
Kr	Lithic tuff breccia	478624e	3521954n	4127f	1.17e-05	3.25e-06	6	7.16e-06	1.51e-05	20
Kr	Lithic tuff breccia	478613e	3522026n	4140f	1.31e-05	2.79e-06	6	9.55e-06	1.67e-05	21
Kr	Andesite lava block in bx	478613e	3522026n	4140f	2.05e-05	1.38e-05	7	5.57e-06	3.98e-05	22
Js?	Squaw Gulch granite	507216e	3504405n	4785f	1.04e-03	6.38e-04	6	1.84e-04	1.87e-03	23
Kse	Salero megabreccia	507216e	3504395n	4785f	2.47e-05	7.85e-06	4	1.59e-05	3.34e-05	24
Kse	Salero megabreccia	507216e	3504400n	4785f	4.64e-05	3.87e-05	4	2.47e-05	1.04e-04	25
Kjd?	Diabase dike	507216e	3504401n	4785f	7.33e-04	0.00e+00	1	7.33e-04	7.33e-04	26
Js?	Squaw Gulch granite	507216e	3504410n	4785f	2.27e-04	1.37e-04	4	5.97e-05	3.41e-04	27
Keqf?	Elephant Head quartz monzonite, fine grained dike	509690e	3503690n	5922f	2.85e-03	4.42e-04	6	2.31e-03	3.33e-03	28
Keqc	Elephant Head quartz monzonite	509690e	3503690n	5922f	3.05e-03	5.95e-04	5	2.28e-03	3.94e-03	29
Keqc	Elephant Head quartz monzonite	509766e	3503855n	6027f	3.91e-04	5.30e-05	5	3.19e-04	4.67e-04	30
Kj	Josephine Canyon diorite (float)	510099e	3504022n	6098f	5.16e-04	0.00e+00	1	5.16e-04	5.16e-04	31
Kj	Josephine Canyon diorite	510099e	3504022n	6098f	2.01e-04	6.27e-05	5	1.33e-04	2.75e-04	32
Kj	Josephine Canyon diorite	510099e	3504012n	6098f	1.65e-04	8.39e-05	3	7.24e-05	2.36e-04	33
Keqc	Elephant Head quartz monzonite	509105e	3504011n	5710f	5.26e-04	1.06e-04	5	3.90e-04	6.52e-04	34
Keqf?	Elephant Head quartz monzonite, fine grained dike	509105e	3504011n	5710f	1.96e-03	2.63e-04	5	1.70e-03	2.35e-03	35

Geologic Setting

The upper Santa Cruz River Valley is in the southern Basin and Range province of southeastern Arizona and northern Sonora (Gettings and Houser, 1997). This terrain of alternating fault-bounded linear mountain ranges and sediment-filled basins began to form at about 17 Ma in southeastern Arizona as the result of dominantly east-northeast/west-southwest directed crustal extension. The topography of the basins and ranges in this part of the province has a zigzag northeast and northwest pattern that may be a result of movement along west-northwest-trending Mesozoic faults that were reactivated by the Miocene extension. The Santa Rita, San Cayetano, and Patagonia Mountains bound the eastern side of the upper Santa Cruz Valley (fig. 1). These mountains are made up of a variety of rocks including igneous, metamorphic, volcanic, and sedimentary rocks ranging in age from Precambrian to Miocene (Drewes, 1971, 1972, 1980; Simons, 1974; pl. 1). Mount Wrightson in the Santa Rita Mountains (fig. 1), at 2,881 m, is the highest point in the area.

The Tumacacori and Atascosa Mountains bound the western side of the valley and are composed chiefly of Tertiary volcanic rocks with the exception of a Jurassic granitic pluton at the northern end of the Tumacacoris (fig. 1; pl. 1). The Pajarito Mountains at the southern end of the valley west of Nogales are composed of Cretaceous volcanic rocks (Drewes, 1980). The mountains west of the valley are considerably lower than those to the east. Sardina Peak in the Tumacacori Mountains is 1,712 m; Atascosa Peak in the Atascosa Mountains is 1,957 m.

The sedimentary rocks in the upper Santa Cruz Valley are Miocene to Holocene, chiefly alluvial sand and gravel deposits of fans, valley centers, terraces, and channels. On the basis of age and consolidation, these rocks can be separated into two basin-fill units overlain by surficial deposits as follows; (1) lower basin-fill unit or Nogales Formation, probably lower and middle Miocene, and poorly to moderately well consolidated, (2) upper basin-fill unit, upper Miocene to lower(?) Pleistocene, and unconsolidated to poorly consolidated, and (3) Pleistocene and Holocene surficial deposits including alluvium of stream channels, flood plains, and terraces,

unconsolidated overall but locally well indurated. Some volcanic flows are intercalated with the basin fill, generally at the top of the Nogales Formation (pl. 1).

The rocks of the study area record a long history of tectonism and magmatism that is described in numerous publications. Dickinson (1989) summarizes the tectonic history of the area at scales appropriate to this study.

Comparison of aeromagnetic data with geologic map data

Detailed comparisons of the mapped geology with the aeromagnetic data were made to establish the magnetic signatures of the various rock units. For most of the area, the correlations were made using 1:48,000 scale geologic maps (Drewes, 1971; Simons, 1974) overlain with contour maps of the aeromagnetic anomaly and complemented with color shaded relief images of the aeromagnetic anomaly at the same scale. This combination proved to be very useful for observing relationships both in the field and in the office. The western part of the area is not covered by detailed mapping and in this part of the study area correlation was made with 1:125,000 scale mapping (Drewes, 1980; Gettings and Houser, 1997). The geologic map of Plate 1 is from 1:125,000 scale mapping and does not include the detail of the 1:48,000 maps but is used here for convenience of presentation. Plate 2 shows the shaded relief aeromagnetic data overlain with the line work from the map of Plate 1. By comparing the two plates it is easy to locate the extent of the various geologic units on the aeromagnetic map. Areas or anomalies of particular interest to be discussed below are numbered on Plate 2.

One caveat must be borne in mind in studying Plate 2 and subsequent plates in this report with geologic linework overlain on them. The geologic base was hand digitized from the map of Drewes (1980) over a period of several years by students, and some registration errors are contained in the data. These errors are not systematic and appear to be small rotations and translations of different digitizing sessions relative to one another. Consequently, the linework is registered to the aeromagnetic map correctly in some areas and not in others. The overlays in this report are the result of carefully fitting (rubber sheeting) the linework to points on the

13

aeromagnetic map determined by overlaying the aeromagnetic data on the original paper map of Drewes (1980). The resulting fit is reasonably good in most areas but some linework is as much as 500 m off from the correct point on the aeromagnetic map. The majority of the linework is believed by the author to be within 300m of its correct location. Correlations with geologic units are not affected by this problem because the associations were made using accurate overlays of the aeromagnetic map on the 1:48,000 and 1:125,000 scale maps and did not make use of the digital linework. The linework overlain on plates 2-7 contains a few spurious lines. The lines present on pl. 1 are to be taken as correct. Appendix 1 contains Postscript files of contour maps of the parts of the aeromagnetic survey which overlay the 1:48,000 maps of Drewes (1971) and Simons (1974). Appendix 1 also contains files to allow plotting 1:175,000 scale versions of color plates 1-7.

In general, there is a good correlation between exposed geologic units and the aeromagnetic anomaly field, with many of the mapped faults displaying a strong magnetic signature, and a number of magnetic anomalies strongly suggest faults not shown on the geologic map. In some places, faults mapped on the surface have no magnetic expression and cut across magnetic features such as anomaly minima and gradients. The aeromagnetic anomaly field is highly varied in the study area and is due to a large variety of lithologies with highly variable magnetization. Aeromagnetic anomalies are very large and have steep gradients in several areas of the map (for example, numbers 1, 6, 9, and 14 on pl. 2) with positive anomalies in excess of 2,000 nanoTesla (nT) (no. 1 on pl. 2) and negative anomalies of —500 nT or more (north of no. 9, pl. 2) indicating strongly magnetic rocks near the surface.

Faults mapped in the basin fill (west of nos. 4 and 16, pl. 2, and pl. 1) do not exhibit short wavelength anomalies indicative of magnetic sources in the surficial basin fill sediments such as are observed in the Albuquerque basin (Grauch, 1997). Instead, their magnitude and wavelength reflect the fault offset of deeper magnetic sources, typically at the bedrock-basin fill interface (Hegmann, 1998; Baldyga, 2000). Generally, the basin fill has behaved as a brittle material and the mapped surface scarp of the fault is approximately the up-dip projection of the fault defined by the aeromagnetic and gravity data, rather than directly above the edge of the upthrown block as would be expected for unconsolidated material (Baldyga, 2000). This is because the Santa

Cruz basin fill is mainly consolidated conglomerate with only a relatively small amount of unconsolidated material (Gettings and Houser, 1997).

Relations between mapped rock units and magnetic anomalies The largest positive anomaly in the study area is centered on the Grosvenor Hills Volcanics (Drewes, 1971; no. 1, pl. 2); a sequence comprised of Oligocene lower rhyolitic and upper rhyodacitic members. The sequence is intruded by several 26-28 Ma rhyodacite and granodiorite laccoliths, dikes and plugs (Drewes, 1971). The exposed laccoliths (no. 1, pl. 2; pl. 1, and Drewes, 1971) are associated with reversely polarized anomalies characteristic of reversely magnetized thin sheets. These anomalies are of the order of 500 nT amplitude and superposed on a large circular positive anomaly of about 1700 nT peak to trough intensity, about 10 km diameter, and approximately centered 2km southwest of no. 1 on pl. 2. The circular anomaly is interpreted to be due to a subsurface intrusion based on the following evidence. First, the circular anomaly shape is larger than the laccoliths and is normal in polarity whereas the laccoliths are reversed; second, the anomaly does not correlate closely with any one unit on the geologic map; and third, the fault pattern on the geologic map (pl. 1) is that of doming and most of the upper part of the Grosvenor Hills Volcanics upper member has been eroded away in the area contained by the anomaly, suggesting doming and uplift. Assuming the circular anomaly to be a thick intrusive, the models of Andreasen and Zietz (1969) give an effective susceptibility of 0.009 cgs/cc, which is quite magnetic. However, if it is assumed that the rocks possess significant remanent magnetization, a susceptibility of 0.003-0.005 cgs/cc gives Konigsberger ratios Q of 2.2-0.9. These are typical values implying the induced and remanent magnetizations are about equal and the intrusion has a susceptibility typical of a fresh basalt. Although no sites were measured in this study on the Grosvenor Hills laccoliths, susceptibilities in the Laramide Josephine Canyon diorite and Gringo Gulch pluton are about 0.003 cgs/cc (table 1). Since the anomalies associated with these bodies (nos. 2 and 11, pl. 2) are less intense than those of the Gosvenor Hills anomaly, it is reasonable to assume that the source of the circular anomaly has a susceptibility in the range 0.003-0.005 cgs/cc and a Q of 1-2. If the laccoliths are assumed to be 250 m thick (the thickest exposed section, Drewes, 1971), the models of Andreasen and Zietz (1969) imply an effective susceptibility of 0.005cgs/cc for these rocks. These susceptibility and Q estimates are in good

15

agreement with average values for rock types of andesitic to basaltic compositions (Clark, 1997 and 1999).

A group of north-northwest positive anomalies are associated with the Laramide intrusive rocks, generally of dioritic composition (for example no. 2, pl. 2). The anomalies are not as intense as those of the Grosvenor Hills but they are nevertheless large amplitude within the study area. These rocks include the Josephine Canyon Diorite, the Madera Canyon granodiorite, and the main phase of the Gringo Gulch pluton (Drewes, 1971; Vugteveen and others, 1981). They are the northern end of a narrow belt of intrusives that have strong positive magnetic anomalies and which extend southward into Sonora, Mexico (Finn and others, 1999). Field measurements of the magnetic susceptibility of these rocks (Table 1) show that they have large susceptibilities (0.001-0.003 cgs/cc), and arguments similar to those above for the Grosvenor Hills intrusion suggest they have a significant remanent magnetization in a normal direction with Q values of the order of 1. The distribution of these rocks is important because intrusions of intermediate to silicic composition of Laramide age are often associated with the large porphyry copper deposits of this region of Arizona.

The Laramide Josephine Canyon Diorite forms the core of the San Cayetano Mountains horst block and its magnetic anomaly forms a nearly north-south ridge in the magnetic field (between nos. 3 and 5, pl. 2). A small stock, the granodiorite and rhyodacite porphyry of the San Cayetano Mountains (Drewes, 1971) is reversely polarized (no. 3, pl. 2). The stock is dated radiometrically (lead-alpha method) at 27 Ma (Drewes, 1971). This age is essentially identical (27.5 Ma, potassium-argon method, Drewes, 1971) with the rhyodacite laccoliths in the Grosvenor Hills intrusion which are also reversely polarized.

The Grosvenor Hills volcanics (Drewes, 1971) contain rocks of both normal and reversed polarities. The rhyolite (older) member is normally polarized (no. 4, pl. 2), while both units of the rhyodacite (younger) member and the laccoliths and dikes intruding them (no. 1, pl. 2) appear to be reversely polarized (nos. 5 and 6 and especially 4 km to the southeast of no. 5, pl. 2). The granodiorite and rhyodacite porphyry stock of the San Cayetano Mountains appears to be

contemporaneous with the extrusion of the rhyodacite member of the Grosvenor Hills volcanics and the intrusion of the laccoliths and dikes.

The Jurassic Squaw Gulch Granite (and quartz monzonite) of Drewes (1971) is present over a large area of the central portion of the survey, from the north end of the San Cayetano Mountains north to Cottonwood Canyon, east almost to Temporal Gulch and south nearly to Patagonia (fig. 1). This body is of batholithic proportions and forms the basement for the Cretaceous volcanic rocks of the Salero Formation (Drewes, 1971) extruded on it. It is reversely polarized (for example, no. 7 on pl. 2). Note the north-northwest extension of this unit in the geologic linework from the 7 on pl. 2; this is the worst registration error found in the linework — the granite should overlie the magnetic low 300-500 m to the east. From the 7 southwards the contact is correctly located. The Salero formation (Drewes,1971) consists of a lower member of mainly dacitic flows and tuff breccias which are reversely polarized, overlain by a rhyodacite welded tuff member which is normally polarized. Between the two lies an exotic block member (Drewes, 1971) or megabreccia which is probably reversely polarized (no. 8, pl. 2; no. 3, table 1) but has some areas of ambiguous magnetic signature on the map of Drewes (1971). Although the area of the Salero Formation just east of the Grosvenor Hills (no. 1, pl. 2) is undivided on the map of Drewes (1971), from the magnetic anomaly it appears to be dominantly reversed, that is, the lower and exotic block member. The large magnetic low (no. 9, pl. 2) on the north side of the large circular anomaly is a compound anomaly, made up in part by the dipole minimum of the (normal) circular anomaly and in part due to the (reversed) Squaw Gulch Granite forming the bedrock in this area.

The Gringo Gulch pluton (no. 11, pl. 2) has a normally polarized anomaly, although in detail it is distorted in the area of outcrops of microgranodiorite (Drewes, 1971) and this late phase unit is reversely polarized as indicated by the measurements (nos. 8-9, table 1; Hagstrum, 1994). The age of the pluton is now accepted as the older of those reported by Drewes (1971) and the volcanic rocks intruded by it are Lower Paleocene (Laramide) in age (Vugteveen and others, 1981). As reported by Vugteveen and others (1981), the Gringo Gulch volcanics are reversely polarized (southwest of no. 11, pl. 2 and no. 12, pl. 2); however the uppermost unit appears to be normally polarized (no. 13, pl. 2). These volcanics apparently include the extrusive rocks of Red

Mountain to the south (fig. 1), although this is ambiguous because of the positive anomaly caused by the Red Mountain porphyry (no. 18, pl. 2) which contains disseminated magnetite and is normally polarized. In addition the volcanic rocks of the Red Mountain area are highly altered and oxidized (Corn, 1975) and thus not very magnetic in any case. The large anomaly east of Red Mountain (east of no. 18, pl. 2) is due to Laramide intrusive rocks of Saddle Mountain (fig. 1) similar to the Josephine Canyon diorite. Similar anomalies can be seen to the south of Red Mountain (no. 18, pl. 2) and are almost certainly caused by similar Laramide intrusives at depth because there is no consistent correlation between exposed units (Simons, 1974) and the strong positive anomalies. In this area, (the western Patagonia Mountains, fig. 1) the horst of Precambrian and Jurassic rocks shown on pl. 1 and corresponding to strong positive magnetic anomalies (north and south of no. 19, pl. 2) may have as its source of uplift the intrusion of the magnetic Laramide rocks.

The biotite-hornblende granodiorite of Paleocene age (Simons, 1974) has a similar large positive anomaly except where the rocks are altered in an east-northeast trending belt (no. 19, pl. 2) that includes the mining areas of Providencia and Sycamore Canyons and Soldier basin (Simons, 1974).

In the northern part of the study area, strong anomalies are present beneath an area of Precambrian granite, Cretaceous sedimentary, and Tertiary intrusive rock outcrop (no. 14, pl. 2). Once again, the anomalies do not correlate well spatially with Precambrian outcrop and the source of the magnetic anomaly may be a mostly buried Laramide intrusion that has rafted the Precambrian rocks upward, similar to the north end of the Whetstone Mountains (Gettings, 1996). The area of the magnetic low is much larger than the mining districts and the areas of alteration mapped by Simons (1974), and the anomaly may identify an underlying porphyry system whose upward apophyses are the mining districts.

The Elephant Head quartz monzonite (Drewes, 1971; no. 15, pl. 2) is reversely polarized (also shown by Hagstrum, 1994) and yields a generally low magnetic anomaly field in the northwest end of the Santa Rita Mountains. However, a positive anomaly (no. 16, pl. 2) is due to Josephine Canyon diorite, a small outcrop of which is mapped (Drewes, 1971) beneath the anomaly maxima.

In the Tumacacori Mountains (fig. 1), the oldest volcanic rocks are andesite flows (Ta, pl. 1); these rocks appear to be normally polarized and continuous at depth in a northwest trending belt (southwest of no. 17, pl. 2). The bulk of the range is made up of younger rhyolitic volcanic rocks, predominantly ash-flow tuffs that are reversely polarized. The Jurassic granite mapped at the north end of the range does not have a strongly correlated magnetic anomaly; there is some suggestion from the map pattern that it could be reversely polarized. The Jurassic granite of Mount Benedict (no. 20, pl. 2) appears to be normally polarized, although it also may be intruded below judging from the mapped fault pattern which is consistent with doming and the fact that it is heavily intruded with dikes (Simons, 1974).

From the above discussion and noting that some of the reversely polarized rocks (table 1; also Hagstrum, 1994) indicate paleomagnetic directions that are not parallel (or anti-parallel) to the present day induction direction, it is clear that in much of the survey area, remanent magnetization is an important, sometimes dominant, component of the magnetic anomaly. Because of this, transformations often performed on aeromagnetic survey data, such as reduction to the pole and various forms of filtering and depth-to-source estimation can only be used with great caution as they are not valid for magnetic fields with remanent magnetization directions other than that of the inducing field. In this survey, many of the magnetic anomaly minima are due to remanent magnetization directions other than the induction direction and thus are not due to nonmagnetic rocks as is often assumed. This renders automatic depth-to-source calculations useless for methods that assume negative anomalies are due to greater depth-to-magnetic-source. This includes the finding of horizontal gradients often performed on potential field data to locate body edges (e.g. Blakely and Simpson, 1986) because the computation for aeromagnetic data requires the reduction to the pole transformation.

Trends in the magnetic survey data and their relation to geologic features Plate 3 displays a set of trend lines drawn by the author using image manipulation software. The trend lines were drawn from visual inspection on the computer screen (21 monitor) using the computer s mouse on the shaded relief image of the aeromagnetic data (pl. 2). The geologic linework was superimposed afterward as a separate layer. Because of parallax effects on the onscreen image, some lines may not be located exactly where they would be had they been drawn on a smaller scale map and digitized. Trends which appeared visually obvious to the author were drawn, and

although and attempt was made to be thorough for trends 2 km or longer in length, certainly some were overlooked, particularly those roughly parallel to a nearby trend already drawn. Comparison with the geologic linework shows that many of the magnetic anomaly trends coincide with geologic contacts or faults or closely parallel them. Phillips (2001) discusses some of the reasons trends may parallel a structure or magnetic boundary but be offset from them. In this study offsets as much as 500 m between a trend line and the structure may be seen on pl. 3. Many of the offsets are due to using the observed (dipole) magnetic anomaly data rather than a reduced-to-the-pole version; however, as discussed above, the reduction-to-the-pole transformation is invalid for much of the dataset. Some faults in the Santa Cruz basin area either have no magnetic expression or such a small one that it was not detected by the author. On the other hand, several faults within basin fill have extensions in the sub-basin bedrock even though the fault has no surface trace along the extension.

Four lines on pl. 3 are heavier in weight than the others, and mark what are believed to be important boundaries based on evidence presented below. The heavyweight boundaries separate the map of pl. 2 into an eastern area of high amplitude, rough anomalies, and a western area of smoother , lower amplitude anomalies. The northwest-trending heavyweight line in the southwest of the map area follows the Santa Cruz fault (Gettings and Houser, 1997) and its extensions. The heavyweight line trending northwest in the northeast part of the map follows a magnetic minima that crosses many structures and is part of a regional magnetic boundary extending both northwest and southeast outside the map area (Finn and others, 1999). This regional-scale magnetic low may mark the accretionary boundary of arc terranes from the southwest and the associated arc magmatism during Late Triassic and Early Jurassic times (Dickinson, 1989). The boundary is offset to the southwest near the north central edge of the map; this is a somewhat arbitrary decision on the part of the author and may be artificial. The final heavyweight line on Plate 3 trends approximately N30°E from the Santa Cruz fault at 31°30 N, 111° E to the north edge of the map. This line and the Santa Cruz fault line define a boundary within which all of the high amplitude anomalies of the Santa Rita and Patagonia Mountains are contained (the areas marked A on pl. 3). This northeast-trending boundary is quite well defined in the aeromagnetic field (see pl. 2), but does not correspond to any single feature on the geologic map (pl. 1). An unresolved question is why the amplitudes of anomalies

should change so abruptly across this boundary from less intense to the northwest to more intense to the southeast. Rocks causing the large positive anomaly in the extreme northwest part of the area (UTM 495 km east, 3515 km north, pl. 3) and to the north of the study area are similar age and composition to the Laramide diorites southeast of the boundary, but do not cause as large amplitude anomalies. If they are simply more deeply buried outside of block A (pl. 3) then why is the boundary not a fault? The heavyweight lines trending northwest (pl. 3), and others that parallel them, though not as continuously, are believed to be deep seated structures which have their origin in the Triassic-Jurassic subduction system that accreted the crust in the study area. Many of these structures have been reactivated through time as faults and loci of magmatism. The heavyweight line trending northwest from UTM 3497 km north, 531 km east (pl. 3) includes the Sawmill Canyon fault zone, believed by Drewes (1981) to be a controlling structure throughout the geologic history of the area.

In order to quantify the trends analysis and determine if they were clustered, the trends of plate 3 were digitized. Curved trends were digitized in segments which were approximately straight. From the resulting dataset segment azimuth, length, and coordinates of the segment center were computed. Figure 2 displays several plots made from this dataset. Figure 2a is a histogram of azimuth of the segments. The distribution is tri-modal, with the most frequent trends being about N40°W, the second most frequent about N65°E, and the least frequent approximately N5-10°E. A narrow peak occurs at N83°W; these correspond to a unique cluster from the doming faults in the Grosvenor Hills volcanics in the center of the map area. The northwest trends correspond both to the original structures aquired during crustal accretion and to subsequent reactivation, particularly the Mid-Tertiary magmatism and extensional deformation event (Dickinson, 1989) which resulted in extension oriented along an axis N60°E. In this area, much of the extension has been accomplished on northwest trending normal faults in addition to some low-angle faults (Gettings, 1994). Moreover, extension was not uniform over the whole area resulting in shear motion on N60°E block boundaries. Within the study area, the Santa Rita block apparently extended farther than the block to the southeast containing the Patagonia Mountains. This resulted in a rotational component extending and rotating the southern Santa Rita block in a clockwise sense, providing a tensional regime for emplacement of the Alto dike swarm and related dikes (Drewes, 1996) which host the lead-silver carbonate vein deposits of the area. Two

21

major faults which bound the Patagonia graben (fig. 1, pl. 1, and UTM 524 km east, 3487 km north on pl. 3) appear to be a boundary between these blocks. Offset of the magnetic anomalies due to the Laramide diorites across these faults suggest about 2.5 km of left-lateral motion. The deep (about 300 m, Cisneros and others, 1999) but areally small basin at the town of Patagonia (fig. 1) may be a pull-apart basin resulting from this process.
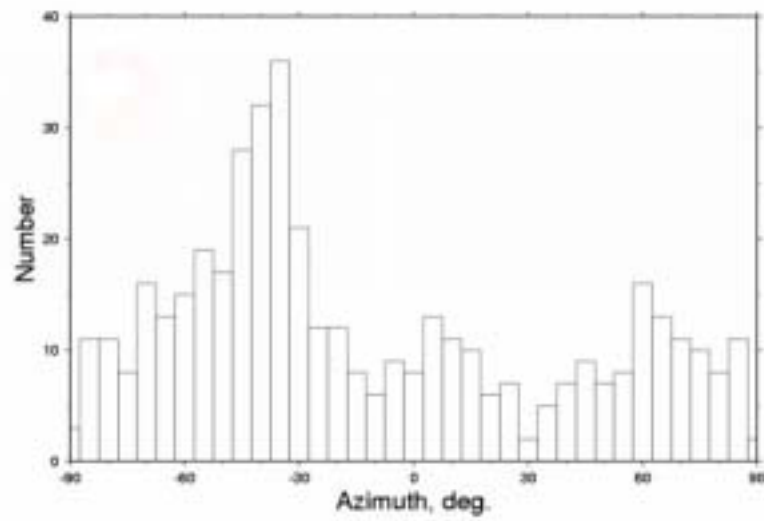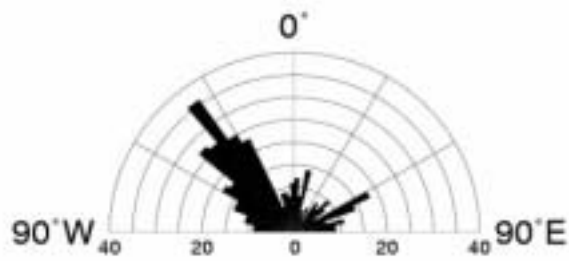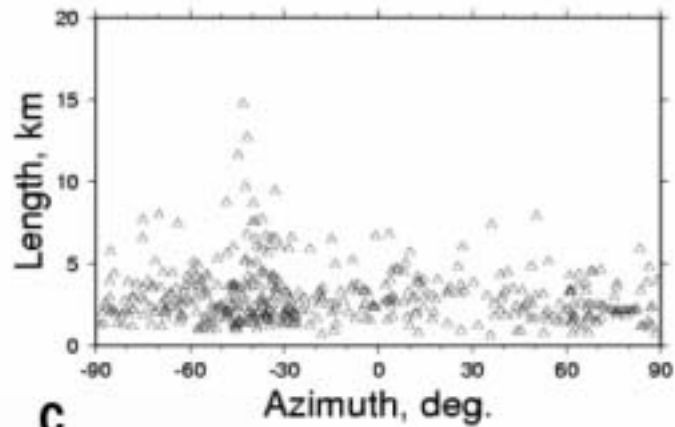
Figure 2. a) Histogram of trend segment azimuths digitized from Plate 3. b) Rose diagram of trend azimuths. c) Plot of trend segment length versus trend segment azimuth.

Figure 2b displays a rose diagram of the observed trends. In this diagram all segments were given equal weight, so it is essentially a radial histogram. The north-trending cluster of trends is clearly displayed on this plot. These trends correspond to the latest deformation, representing east-west extension resulting in north trending faults of the Late Cenozoic Basin and Range episode (Dickinson, 1989).

Figure 2c is a plot of segment length versus segment azimuth. Although it is somewhat misleading because long continuous segments that were not straight were broken into smaller straight line segments, the plot still places a lower bound on trend length as a function of azimuth. The plot shows clearly that the longest straight segments are oriented N40°W, and segments in the 1-4 km length range are essentially uniformly distributed. Segments in the 5-10 km length range occur mainly at the azimuths of the peaks in the azimuth distribution (fig. 2a).

Another technique, closely related to textural measures (discussed below) but difficult to quantify, is to use an image manipulation program to produce an image of the gridded data using random colors (oil slick diagram , D. Clark, oral communication, 1999) as shown in plate 4. This often enables the visual detection of trends in the data as they cross areas of widely varying anomaly texture because it removes the dominating effect of anomaly amplitudes and polarities. Trends that are difficult to trace across magnetically flat areas in the data can sometimes be estimated with this technique. A number of trends so identified are labeled on plate 4 using lower case letters. The letter a identifies the northeast trending boundary discussed above dividing high amplitude anomalies to the southeast from lower amplitude ones to the northwest. Lines labeled b are northwest trending boundaries discussed above. Note that the continuity of these boundaries is easier to see in this display (pl. 4) and that there are several more than identified on plate 3. Not all such boundaries are labeled on plate 4. The line labeled c on plate 4 corresponds to the boundary including the Sawmill Canyon fault zone discussed above and may represent an approximate northeastern boundary of Jurassic crust in this area. The lines labeled d outline the belt of Laramide diorite intrusives, and the line labeled e includes the southern boundary of the Santa Rita block passing through the town of Patagonia, and its extension to the southwest. The visualization of the data shown in plate 4 also shows some areas of essentially uniform texture in color, size, and shape of features. Several of these areas have been outlined and numbered on plate 4. the areas numbered 1 correspond to the volcanic rocks

of the Tumacacori Mountains and their northward extension in the subsurface. The outline of this texture in the Tumacacori Mountains area of plate 4 includes areas along the eastern edge of the volcanic field which are buried beneath basin fill of the Santa Cruz Valley. The outline in the southwest corner of the study area labeled 2 is an area discussed in more detail below. The southwest third of the outlined area is Cretaceous rhyolite lava flows, tuffs, and volcaniclastic sediments (Drewes, 1980) and is thought to be part of a Cretaceous caldera by Lipman and Sawyer (1985). As shown below, the two thirds of the outlined area to the northeast may be the (buried) remainder of the caldera, based on the continuity of textural measures of the magnetic field.

Inferences from textural measures of the aeromagnetic data

Textural measures of potential field data   Another objective of this study was to map textural measures (Gettings, 1999) of the aeromagnetic anomaly field that might be related to rock lithologies and thus be of use in elucidating the geologic structure. Common univariate statistical measures do not characterize texture because they describe integrative properties of the function (fig. 3). Several investigators (for example, Pilkington and Todoeschuck, 1993; Gettings and others, 1991) have shown that the distribution of magnetic anomalies and magnetic susceptibility are fractal in nature and thus highly variable. The fractal character comes from the geologic distribution of the sources which is then mirrored in the potential field anomalies. The fractal dimension characterizes a distribution, but measurement of the dimension for potential field data proves to be quite difficult. This is because potential field data are not self-similar but instead are self-affine fractals, and the dimension is not defined uniquely. In fact, these distributions are mutifractal and possess a spectrum of dimensions (Feder, 1988). Gettings (1999) and Gettings and Bultman (1997) have shown that two robust measures of texture are the normalized number of peaks and troughs and the normalized Euclidean length of the data in a window moving over the dataset. The number of peaks and troughs provides a measure of the roughness of the data while the Euclidean length measures the amplitude of the data. Thus, for the aeromagnetic data, the Euclidean length is a measure of the intensity of magnetization and the number of peaks and troughs is measure of the number and distribution of sources.
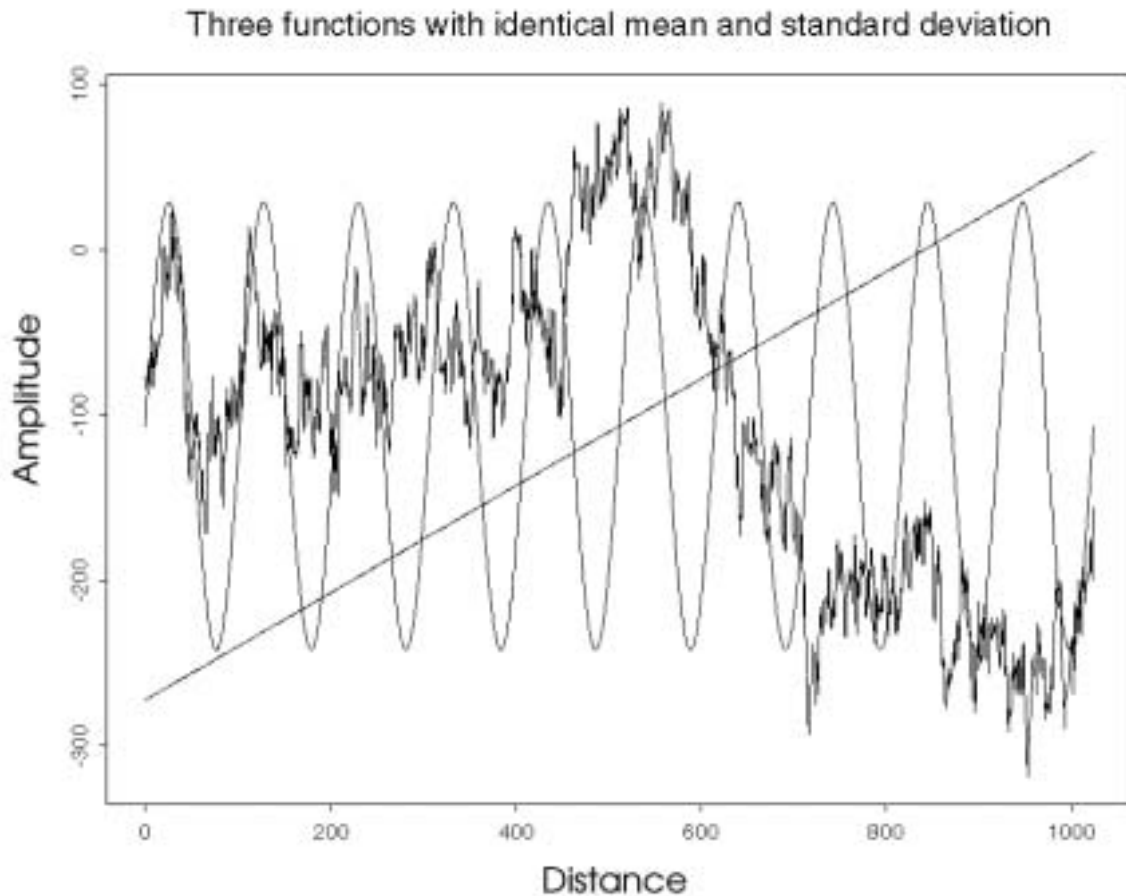
Figure 3. Three functions with identical mean and standard deviation: a straight line, a sine function, and fractional Brownian motion (Feder, 1988) with a dimension of 1.70.

All computations are performed on the flight line data, rather than on some filtered derivative product such as a grid, in order to minimize loss of information content from processing.   The general strategy is to compute the desired quantities along flight lines and then interpolate the results onto a regular grid for map presentation. In practice, this was accomplished by computing all measures of interest on the data in a single, compute intensive, pass through the data which produced a very large output dataset that was analyzed in multiple ways.

Moving window processing The survey data are organized into concatenated flight lines in a single large file. The processing program processes one flight line at a time by repeatedly

26

passing a moving window over the data and computing the various measures within the window. The sizes of the windows and their movement down the flight line (that is, the amount of overlap of successive windows) can be controlled by the user. For each window width, the window was moved from one end of the line to the other in overlapping increments. Maximum delineation of textural boundaries (resolution) is achieved by moving the window only one data point at a time (maximum overlap); however this becomes very compute intensive and in practice the window is moved some larger fraction of the window width for each calculation, such as 200 m or one half or one quarter of the window width. A version of the software (in FORTRAN language) used to calculate the measures is given in Appendix 2.

Within every window, several statistical, textural and wavelet fit measures are calculated. Output consists of the x and y coordinates of the window center (ordinarily UTM easting and northing), the width of the window in km and in number of data points, and the aeromagnetic field minimum, maximum, mean, and standard deviation. Three textural measures are calculated for the data within the window. These are the number of peaks and troughs, the Euclidean length of the data, and the range of the aeromagnetic data divided by its standard deviation. The Euclidean length is a measure of the amplitude of the data and is the square root of the sum of the squares of the successive differences in distance (Δx) and magnetic anomaly (ΔT) across the window.

This measure has mixed units of the square root of km squared plus nanoTeslas squared and thus is not a true length. The name Euclidean length was given to this measure by Gettings (1999) to avoid confusion with a true length. In order to make measures comparable between different window sizes, the Euclidean length and number of peaks and troughs are normalized by the window width X_w so that they are in units of length per km or peaks and troughs per km. Figure 4 shows an example of the calculation of Euclidean length and number of peaks and troughs for two successive windows.

27
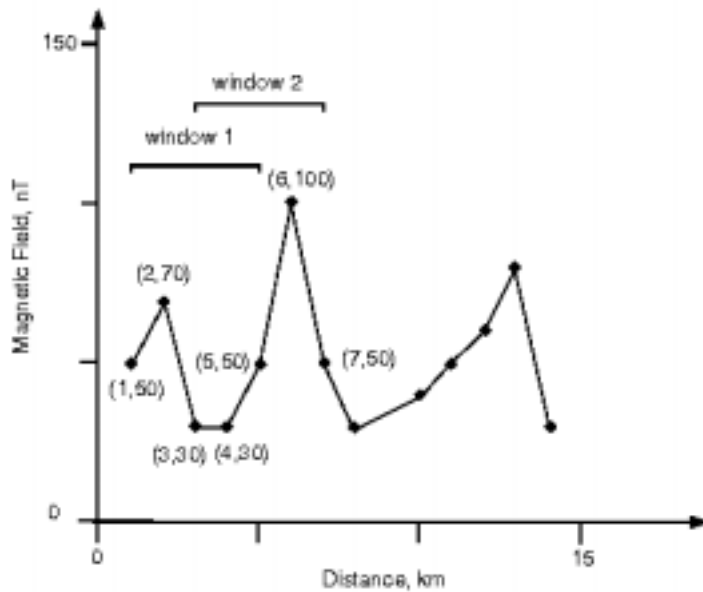
window 1: (5 points, 4 km width)

    number of peaks and troughs = 2 / 4 km = 0.5 per km

    Euclidean length = $\{[(2\text{-}1)^2+(70\text{-}50)^2]^{1/2}+[(3\text{-}2)^2+(30\text{-}70)^2]^{1/2}+$
    $[(4\text{-}3)^2+(30\text{-}30)^2]^{1/2}+[(5\text{-}4)^2+(50\text{-}30)^2]^{1/2}\} / 4$ km
    $= 20.27\ [nT^2+km^2]^{1/2}/km$

window 2: (5 points, moving over 2 points in distance, 4 km width)

    number of peaks and troughs = 1 / 4 km = 0.25 per km

   Euclidean length = $121.04\ [nT^2+km^2]^{1/2}/\ 4$ km
    $= 30.26\ [nT^2+km^2]^{1/2}/\ km$

Figure 4. Example of the calculation of the textural measures of number of peaks and troughs per km and Euclidean length per km for two successive windows five points wide moving two data points at a time.

The ratio of range to standard deviation (often termed R/S, Feder, 1988) is a normalized measure of variability which can be used to estimate the fractal dimension at various scales (window sizes). The Euclidean length divided by the twice the number of peaks and troughs, a measure of mean anomaly amplitude, is also calculated. Finally, a wavelet of a specified shape

may also be fit to the data in the window (not done in this study). The window is then moved by the specified increment and calculations repeated. At the end of a line for a given window size, mean and standard deviation of R/S are calculated and the window size changed by the specified amount, and so on. The procedure is repeated for each line. Partial windows at the ends of lines with total number of points not evenly divisible by the window size are calculated as smaller windows of the remaining number of points. This can lead to gaps in the processing in map view if the survey has lines which end in the interior of the survey area and are completed by other lines beginning where the former line left off.

Results for one line of an aeromagnetic survey To see the properties of these measures, the methods outlined above applied to a single flight line of aeromagnetic survey data will be examined. Figure 5 shows a plot of the magnetic anomaly versus distance for a single flight line. The data show a highly variable and magnetic terrane to the west, a central zone of smooth, smaller amplitude anomalies, and a western zone of larger and rougher anomalies. The computational procedure outlined above was applied for windows from 260 (5.2 km) points to 20 (400m) points in width, moving 10 points (200m) at a time.
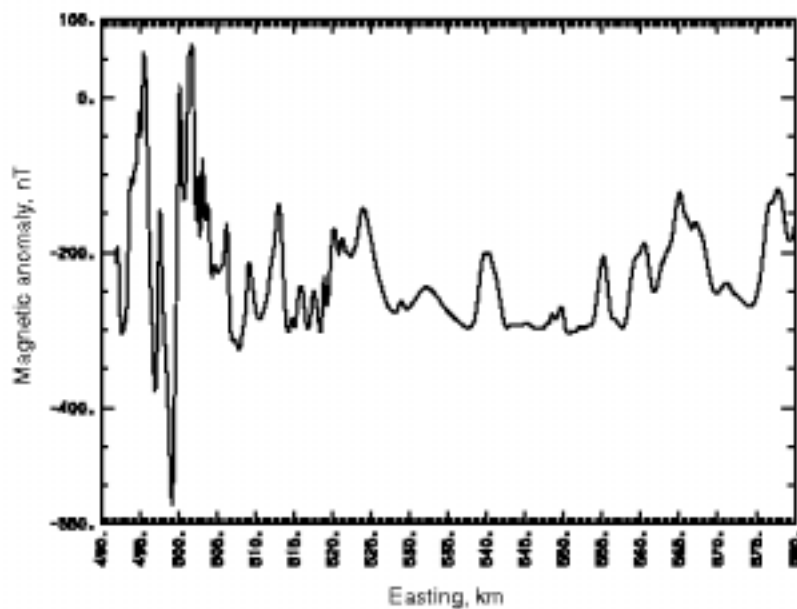
Figure 5. Aeromagnetic anomaly data from one line of a high resolution aeromagnetic survey.

Textural measures of the data of figure 5 are shown in figure 6 for the number of peaks and troughs per km and in figure 7 for the Euclidean length per km for four window widths. Study of these figures demonstrates that the window width is not a first order variable and any peak at a larger window width is also present at higher resolution at a smaller window width. For the textural measures, then, it is only necessary to consider the measures at the window width appropriate for the smallest geologic structure of interest.
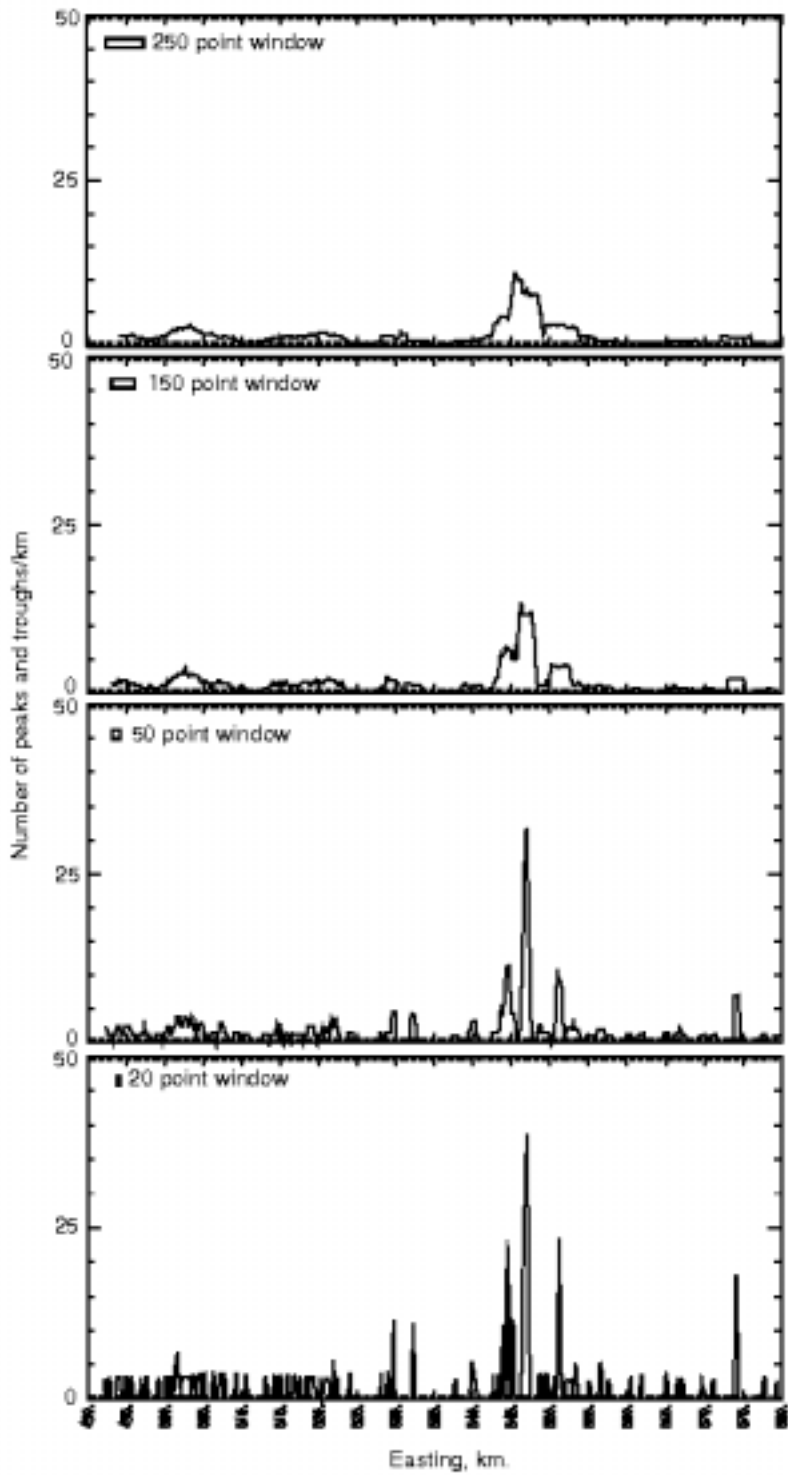
Figure 6. Number of peaks and troughs per km for the data of figure 5 for four different window widths. Spacing between data points is about 20 m.
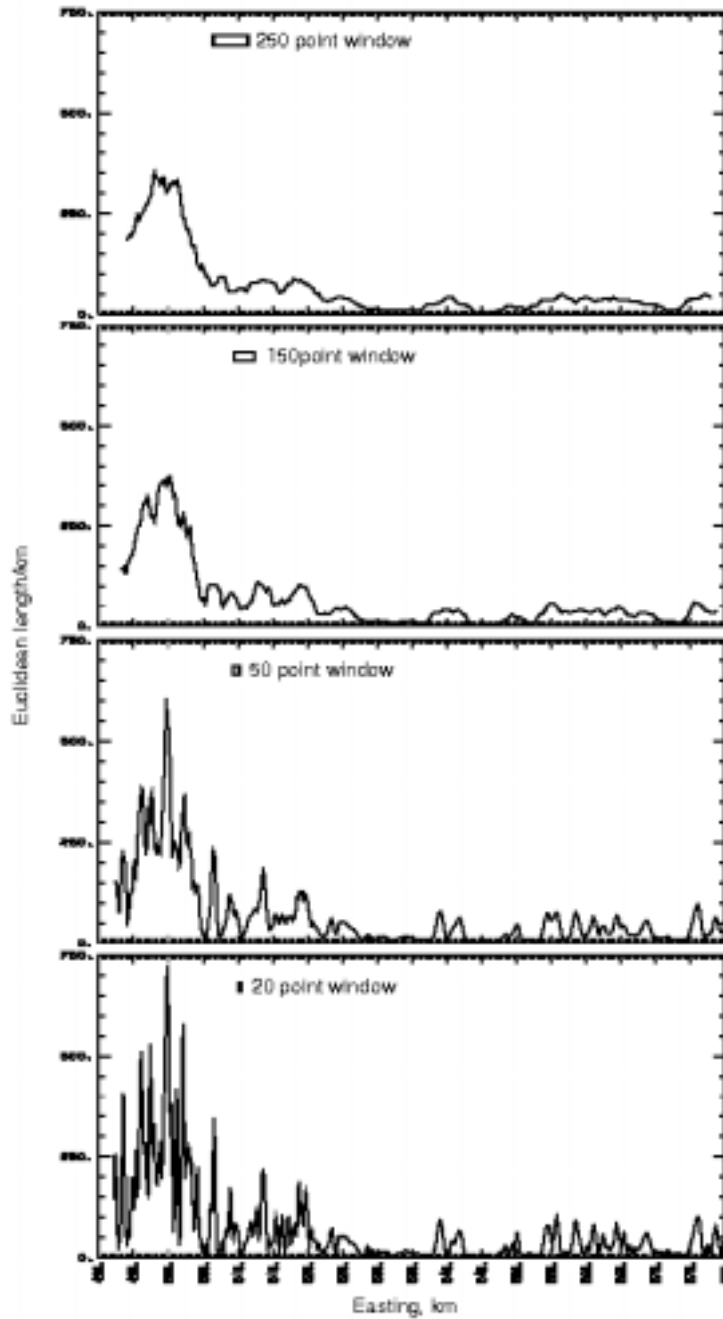
Figure 7. Euclidean length per km in units of the square root of km squared plus nanoTeslas squared for the data of figure 5 for four different window widths. Spacing between data points is about 20 m.

In figure 6, the number of peaks and troughs is characterized by about 3/km for the western 40% of the profile, and less than 1/km for the eastern 60% which has clusters of higher values superposed on it. At about 545 km several large peaks are present denoting very noisy data even though the amplitudes of the anomalies are very small as shown on figure 7 and on figure 5.

The Euclidean length per km, figure 7, shows a large peak in the western 20% of the profile with a moderate cluster of peaks immediately to the east. These reflect the large amplitude, relatively noisy (many peaks and troughs) anomalies in figure 5. Amplitudes are relatively small in the central part of the profile, and there are moderate amplitude anomalies in the eastern third of the data profile.

Number of peaks and troughs per kilometer The number of peaks and troughs per kilometer computed as described above on the flight line profiles and then converted to a grid using minimum curvature (Webring, 1981) is shown as a colored image in Plate 5. The geologic map line work has been overlain for reference as in previous plates. The average spacing between observations for this dataset is 9 m; a 200 point window was used to define textural differences of about 1.8 km extent or larger. Window overlap was 0.1 the window width or 180 m on average. One result of using such a large window is to remove the effects of shorter spatial wavelength anomalies; in general, these are the effects of near-surface sources.

The area of large amplitude anomalies in the central part of the map is generally an area of relatively few peaks and troughs, and the areas of JTrvs in the northeast part of the map (pl. 1 and pl. 5) are generally the smoothest areas of all. Some areas of Tertiary conglomerate and basin fill also have few peaks and troughs, although some areas of both unconsolidated fill and conglomerate have large numbers of peaks and troughs (no. 1, pl. 5). These areas may be loci of deposition of rocks of igneous (magnetic) provenance within the basin fill. Alternatively, they could be due to volcanic flows within or beneath basin fill. This is less likely, however, because areas of obvious extension of volcanic flows from the Tumacacori Mountains into the basin fill are not characterized by such a large number of peaks and troughs per km (for example, the area about 5 km southwest of 1 on pl. 5). The good correlation with the Santa Cruz younger gravels

(basin fill) in plate 5 (no. 1) probably reflects sources of magnetic detritus from tributary canyons from the Tumacacori and Santa Rita Mountains.

The area outlined in the southwest part of the map (no. 2, pl. 5) has a large area of large number of peaks and troughs over an area of both outcropping bedrock and basin fill. Because the boundary of this area crosses several lithologies and does not correlate well with the basin fill, it is here inferred that the portion of the area outlined that is beneath basin fill represents the downfaulted portion of a rhyolite caldera. To the southwest, within the outlined area (no. 2, pl. 5) are exposed rhyolitic rocks (pl. 1) identified as part of a Mesozoic caldera by Lipman and Sawyer (1985).

In the central part of the map area, the high amplitude anomalies of the Grosvenor Hills volcanics (no. 3, pl. 5) and the Laramide intrusives (no. 3, pl. 5) to the northeast have only moderate to few peaks and troughs per km, but they are not distinguished from each other by this measure. The extrusive tuffs of the Salero Formation (Drewes, 1971) do correlate well with areas of large number of peaks and troughs (pl. 1 and pl. 5).

In the extreme northeast, a large area of large number of peaks and troughs (pl. 5) appears to correlate with the drainage pattern and alluvium. To its south however, several northwest trending belts of large number of peaks and troughs occur (no. 5, pl. 5) and cut across the alluvial and drainage pattern onto bedrock. These areas appear to correlate with Laramide and Lower Cretaceous volcanic rocks of andesitic to rhyolitic composition (pl. 1), although the correlation is somewhat ambiguous. The patterns may therefore be caused by magnetic sources beneath those exposed at the surface. It should be noted that these areas occur along steep gradients on the anomaly map (pl. 2) and would not be detected without examining the number of peaks and troughs measure.

Finally, the Tumacacori Mountains volcanics (no. 6, pl. 5) display a distinctive and coherent pattern on plate 5. The pattern clearly extends outside the area of outcrop eastward into the Santa Cruz Valley along much of the mountain front. This suggests the volcanic flows are present in much of the subsurface of the western Santa Cruz Valley.

Euclidean length per kilometer The Euclidean length per kilometer computed as described above on the flight line profiles and then converted to a grid using minimum curvature (Webring, 1981) is shown as a colored image in Plate 6. The geologic map line work has been overlain for reference as in previous plates. This parameter essentially measures strength of magnetization for the rocks within the window because the window width stays constant. Thus, large anomalies give large Euclidean lengths and small anomalies give small values.

The areas in plate 5 (no. 1) appear on plate 6 (no. 1) as areas of small Euclidean length per km, adding weight to the interpretation that they are due to magnetic detritus at shallow depths. If they were due to deep sources, they would likely not show up in either measure because of their small amplitude.

Area no. 2 (pl. 6) conforms closely to the area of the same label in plate 5 and confirms that this is an area of homogenous anomaly signature, here believed to be the downfaulted portion of the Cretaceous rocks exposed to the southwest (Kr, pl. 1).

The large amplitude anomalies of plate 2 show up as areas of large Euclidean length per km (no. 3, pl. 6) but the area of Cretaceous Salero Formation tuffs (mostly normally polarized) lying on the reversely polarized Squaw Gulch granite (Drewes, 1971) appear as large Euclidean length per km anomalies. This area is north of the ‟3‟ on plate 6 on the north side of the ‟ Salero fault zone (also see pl. 1). The Salero fault zone is the long, northwest trending fault just south of the ‟ 2‟ on pl. 2 and north of the ‟9‟ on plate 2. The entire area of the Santa Rita-Patagonia Mountains block as outlined in the trend analysis section above (area ‟A‟, pl. 3) is delineated as an area of high magnetization.

The Tumacacori Mountains volcanics appear as a fairly distinctive area of larger Euclidean length per km anomalies. Comparison with plate 2 shows that the larger values occur over strongly reversely polarized rocks. Extensions of the volcanic rocks in the subsurface of the Santa Cruz Valley basin fill are obvious.

The two areas marked 5 on plate 6 are both areas interpreted to be areas of shallow depth of basin fill. These areas are westward extensions of exposed bedrock to the east and are important target for mineral exploration because the exposed bedrock areas contain numerous base and precious metal occurrences.

Ranked Euclidean length and number of peaks and troughs

The number of peaks and troughs grid and the Euclidean length grid can be combined in a number of ways. For this study, a simple ranking scheme was used to produce a rank for each node of the two grids depending on the length value and number of peaks and troughs value at that node. In the matrix below, number of peaks and troughs increases with increasing column number and Euclidean length increases with increasing row number. For these data the distribution of both number of peaks and troughs and Euclidean length were divided into four bins. Ranks were assigned as integers between 1 and 16 as shown in the matrix table below (fig. 8). For the scheme used, relatively many peaks and troughs and large Euclidean length receive a high rank and few peaks and troughs and small length gets a smaller rank.
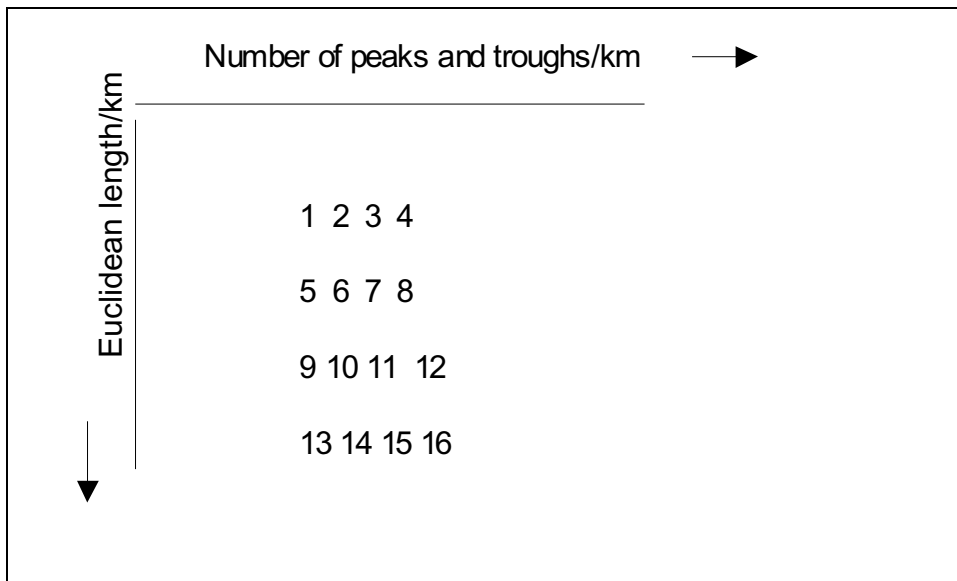
Figure 8. Matrix diagram showing the ranking scheme used to categorize the number of peaks and troughs grid and the Euclidean length grid into a single grid.

This combination is shown in the ranked color image of plate 7. The geologic map line work has been overlain for reference as in previous plates. The rank values are displayed as a color scale using a default color scheme. Study of the color scale on plate 7 shows that much of the ranking of interest (that is numbers 5 through 16) is compressed into the warm red colors. A better color scheme would probably reveal more information in the image. For example, in plate 7 it is difficult or impossible to tell a value of 8 (many peaks/troughs but intermediate amplitude) from a 13 (few peaks/troughs and largest amplitudes).

In plate 7, a consistent background texture for the whole of the study area has been identified (blue/dark blue on pl. 7) corresponding to the average crustal magnetic signature. Superimposed on this are areas of subsequent igneous activity. Numerous places of extensions of textural measures from on bedrock to beneath basin fill are detected (for example, nos. 1, pl. 7) thus mapping lithology beneath the cover.

The Jurassic granite at the north end of the Tumacacori Mountains is discriminated from the volcanic rocks and appears to extend in the subsurface to the north and west (no. 2, pl. 7).

As on the two component images (pl. 5 and pl. 6) the areas of magnetic detritus deposition in the Santa Cruz Valley are well delineated (no. 3, pl. 7).

In the southwest of the map area (no. 4, pl. 7), the area of uniform textural measure is well delineated, with superimposed small anomalies from sediments in major washes. The arm off to the west may not be part of the same lithology as it does not have as uniform a texture as the rest of the outlined area.

The Grosvenor Hills intrusion appears as a crude ring of high values surrounding intermediate values over the intrusive body (no. 5, pl. 7).

The upper Salero Formation ash flow tuffs appear as an area of uniform texture with high values, different from the lower member that has intermediate to small values (no. 6, pl. 7).

In the northeast part of the map (no. 7, pl. 7), there is a large area of uniform texture crossing several lithologies. It is not clear what the texture represents, but it is part of the northwest trending major boundary discussed above (pls. 3 and 4) that may be a northeastern boundary for the Triassic-Jurasssic island arc terrane.

Some areas of the Jurassic-Triassic volcanics and overlying Cretaceous volcanic appear magnetically distinct (no. 8 and to the northwest, pl. 7). These are presumably facies and/or compositional variations within the volcanic sequence as the areas of consistent texture follow stratigraphic strike.

The Jurassic granite of Mt. Benedict is similar to the Jurassic granite at the north end of the Tumacacori Mountains except in the eastern fault block (no. 9, pl. 7), supporting the interpretation that the Mt. Benedict block has been intruded by a later magma in times of normal polarity, probably a Laramide age intrusive.

An extensive area of uniform texture consisting of a large number of peaks and troughs and small Euclidean length (no. 10, pl. 7) occurs in the extreme northeast corner of the map. Although the area does not correlate exactly with present day washs (pl. 7, pl. 1), the pattern suggests that the sources are alluvial in origin and perhaps these represent paleochannels filled with detritus that is on the average more magnetic.

Conclusion

Detailed correlation of the aeromagnetic survey data with geologic maps at several scales has produced a wealth of insight into the geologic history and structure of this geologically very complex area. At least three distinct periods of reversed geomagnetic polarity from Jurassic to Cenozoic times are required to explain the observed magnetic anomaly field. Measurements of magnetic susceptibility and remanent polarity of outcrops were invaluable in sorting out which

rocks could explain observed magnetic anomalies and which are due to buried sources. In several cases the magnetic anomaly data are able to confidently predict rock unit identities in areas where they are undifferentiated in the geologic mapping. Several areas of mineral resource potential have been identified and several areas of interest for further geological and geophysical studies have been found. For example, the Gringo Gulch pluton has been shown to both a normally polarized and a reversely polarized phase and detailed dating studies might accurately date the geomagnetic field reversal. Detailed study of the Laramide intrusives using the techniques of magnetic petrology (Clark, 1999) holds promise for evaluation of these rocks as hosts or sources of ore deposits.

Analysis of trends in the magnetic anomaly data correlated with mapped faults and boundaries have quantified major structural directions associated with the major tectonic events in the geologic history of the study area. In particular, penetrative structures probably associated with original formation of the crust in the Triassic-Jurassic magmatic arc event have been identified. These structures are important because they control loci of subsequent magmatism and mineralization. Further study of these trends and associations is merited and would yield further insight into geologic development of this mineral-rich area.

The use of textural measures in the analysis of the aeromagnetic survey data to infer structure is a useful procedure because it emphasizes properties that are difficult to see in the data with traditional representations such as shaded relief images and contour maps. The measures of number of peaks and troughs per km and Euclidean length provide filters which allow comparison of texture in areas of large anomalies with areas of small ones; in traditional displays the large amplitudes dominate and obscure the areas of smaller anomalies. The process of ranking incorporates both roughness (number of peaks and troughs/km) and amplitude (Euclidean length/km) into one image. More research needs to be done on the display of the ranked values to better show all the information contained in the ranking. A principal component analysis type of approach and better display schemes (such as peak/troughs in blue channel and Euclidean length in red channel) should be investigated in future studies. In addition, it would be desirable to incorporate some kind of downward continuation correction for deeper sources to make this a really valuable tool for mapping buried lithology.

By using a window size that defines the minimum size feature of interest together with the textural measues, the shallow trends and dominant features in the data are removed and textures and features of larger areas are displayed. For example, the centers of igneous activity (mainly Laramide and Tertiary) are well delineated (pl. 7). Trends and textures of underlying older crust that are subtle in the data because of the dominance of larger features are revealed. Areas of similar magnetic texture, inferred to represent similar lithology, are mapped until buried too deeply, even though overlain by younger units of varying magnetic character and polarity.

Finally, although emphasizing certain aspects of the data, like any other derivative procedure, the textural measures help one to identify the features in the original data itself. If features in the derivative maps cannot be seen in the original data, they may be artifacts of computation rather than expressions of geologic structure.

References Cited

Andreasen, G.E., and Zietz, I., 1969, Magnetic fields for a 4x6 prismatic model: U.S. Geological Survey Professional Paper 666, 9 p., 210 pl.

Baldyga, C.A., 2000, Relationship of faults in basin sediments to the gravity and magnetic expression of their underlying fault systems: Tucson, University of Arizona Department of Mining and Geological Engineering M.S. Thesis, 113 p.

Blakely, R.J., and Simpson, R.W., 1986, Approximating edges of source bodies from magnetic or gravity anomalies: Geophysics, v. 51, no. 7, p. 1494-1498.

Carmichael, R.S., 1982, Magnetic properties of minerals and rocks, *in* Carmichael, R.S., ed., Handbook of Physical Properties of Rocks, Volume II: CRC Press, Boca Raton, Fla, 345 p.

Cisneros, G., Dearman, M.M., Dodds, B.E., Edwards, N.K., El-Kaliouby, H., Gajda, C.E., Henley, M.L., Killian, J.R., Kyselka, R.C., Moore, J.R., Mwape, F., Philbin, J.J., Phiri, A.C., Reed, B.W., Sorgenfrei, M.M., Sternberg, B.K., Weston, E.A., 1999, Geophysical Surveys near Patagonia, Arizona, Geophysics Field Camp 1999: University of Arizona Department of Mining and Geological Engineering Report LASI-99-1, 66 p.

Clark, D.A., 1997, Magnetic petrophysics and magnetic petrology: aids to geological interpretation of magnetic surveys: AGSO Journal of Australian Geology and Geophysics, v. 17, p. 83-103.

Clark, D.A., 1999, Magnetic petrology of igneous intrusions: implications fo exploration and magnetic interpretation: Exploration Geophysics, v. 30, p. 5-26.

Corn, R.M., 1975, Alteration-mineralization zoning, Red Mountain, Arizona: Economic Geology, v. 70, p. 1437-1447.

Dickinson, W.R.,1989, Tectonic setting of Arizona through geologic time, *in* Jenney, J.P., and Reynolds, S.J., eds., Geologic evolution of Arizona: Arizona Geological Society Digest 17, p. 1-16.

Drewes, Harald, 1971, Geologic map of the Mount Wrightson Quadrangle, southeast of Tucson, Santa Cruz and Pima Counties, Arizona: U.S. Geological Survey Miscellaneous Geologic Investigations Map I-614, scale 1:48,000.

Drewes, Harald, 1972, Cenozoic rocks of the Santa Rita Mountains, Southeast of Tucson: U.S. Geological Survey Professional Paper 746, 66 p.

Drewes, Harald, 1980, Tectonic map of southeastern Arizona: U.S. Geological Survey Miscellaneous Investigations Series Map I-1109, 2 sheets, scale 1:125,000.

Drewes, Harald, 1981, Tectonic map of southeastern Arizona: U.S. Geological Survey
Professional Paper 1144, 10 pl., 96 p..

Drewes, Harald, 1996, Geology of Coronado National Forest, Chapter B, *in* Mineral Resource
Potential and Geology of Coronado National Forest, southeastern Arizona and
southwestern New Mexico: U.S. Geological Survey Bulletin 2083-A-K, p. 17-41.

Feder, J., 1988, Fractals: Plenum Press, New York, 283 p.

Gettings, M.E., 1999, Using textural measures of aeromagnetic data to infer lithology [abs.]:
International Union of Geodesy and Geophysics XXII General Assembly Abstracts,
Birmingham, England, Week A, p. A.390.

Gettings, M.E., 1994, Some structural features along the Tucson-Mogollon Corridor inferred
from gravity and magnetic anomaly data [abs.]: USGS Circular 1103 - A, [Program and
abstracts for 1994 McKelvey Forum], p. 38-39.

Gettings, M.E., 1996, Aeromagnetic, radiometric, and gravity data for Coronado National
Forest, Chapter D, *in* duBray, E.A., ed., Mineral resource potential and geology of
Coronado National Forest, southeastern Arizona and southwestern New Mexico: U.S.
Geological Survey Bulletin 2083-A-K, p. 77-101.

Gettings, M. E., Bultman, M. W., and Fisher, F. S, 1991, Detailed profiles of southeastern
Arizona obtained by a truck-mounted magnetometer - a step toward better utilization of the
information content of geophysical data [abs.]: U.S. Geological Survey Circular 1062, p.
31-32.

Gettings, M.E., and Houser, B.B., 1997, Basin geology of the upper Santa Cruz Valley, Pima
and Santa Cruz Counties, southeastern Arizona: U.S. Geological Survey Open-File Report
97-676, 40 p.

Gettings, M.E., Fisher, F S., Gettings, P.E., and Luedke, R.E., 1994, Some magnetic properties
of rocks from the Silverton Caldera area, Western San Juan Mountains, Colorado: U.S.
Geological Survey Open-File Report 94-291.

Gettings, M.E., Bultman, M.W., and Fisher, F.S., 1993, Geophysical investigations in the search
for covered mineral deposits: Society of Economic Geologists Integrated Methods in
Exploration and Discovery Conference, Denver, Colorado, Program and extended
abstracts, p. AB35-AB36.

Gettings, M.E., Bultman, M.W., 1997, Detailed ground magnetic anomaly profiles used in
delineation of southwest U.S. basin structure [abs.]: International Association of
Geomagnetism and Aeronomy 8th Scientific Assembly Abstracts, Uppsala, Sweden, p. 515.

Grauch, V.J.S., 1997, Aeromagnetic expression of intra-basinal faults in the Albuquerque basin,
New Mexico, USA   [abs.]: International Association of Geomagnetism and Aeronomy 8th
Scientific Assembly Abstracts, Uppsala, Sweden, p. 515.

Hagstrum, J.T., 1994, Remagnetization of Jurassic volcanic rocks in the Santa Rita and
Patagonia Mountains, Arizona: implications for North American polar wander: Journal of
Geophysical Research, v. 99, p. 15,103-15,113.

Hegmann, M., 1998, Gravity and magnetic surveys over the Santa Rita fault system,
southeastern Arizona: Tucson, University of Arizona Department of Geosciences, M.S.
Thesis, 111 p.

Lipman, P.W., and Sawyer, D.A., 1985, Mesozoic ash-flow caldera fragments in southeastern
Arizona and their relation to porphyry copper deposits: Geology, v. 13, p. 652-656.

Phillips, J.D., 2001, Processing and interpretation of aeromagnetic data for the Santa Cruz
basin-Patagonia Mountains area, south-central Arizona: U.S. Geological Survey Open-File
Report 02-98.

Pilkington, M., and Todoeschuck, J.P., 1993, Fractal magnetization of continental crust: Geophysical Research Letters, v. 20, no. 8, p. 639-641.

Simons, F.S., 1974,Geologic map and sections of the Nogales and Lochiel Quadrangles, Santa Cruz County, Arizona: U.S. Geological Survey Miscellaneous Investigations Series Map I-762, scale 1:48,000.

Sweeney, R.S., 2000, Three aeromagnetic surveys in south central Arizona: a web site for distribution of data (on-line edition): U.S. Geological Survey Open-File Report 00-155 (URL:http://greenwood.cr.usgs.gov/pub/open-file-reports/ofr-00-155/scarizona.html).

Vugteveen, R.W., Barnes, A.E., and Butler, R.F., 1981, Paleomagnetism of the Roskruge and Gringo Gulch volcanics, southeast Arizona: Journal of Geophysical Research, v. 86, pp 4021-4028.

Webring, M., 1981, MINC-A gridding program based on minimum curvature: U.S. Geological Survey Open-File Report 81-1224.